Li *et al. Microstructures* 2024;4:2024004
DOI: 10.20517/microstructures.2023.53

Microstructures

Research Article

Open Access

Misfit strain-misfit strain phase diagram of (110)-oriented ferroelectric $PbTiO_3$ films: a phase-field study

Hui-Mei Li[1,2,#], Heng Zhang[1,#], Yu-Jia Wang[1], Yun-Long Tang[1], Yin-Lian Zhu[3], Xiu-Liang Ma[3,4]

[1]Shenyang National Laboratory for Materials Science, Institute of Metal Research, Chinese Academy of Sciences, Shenyang 110016, Liaoning, China.
[2]School of Materials Science and Engineering, University of Science and Technology of China, Shenyang 110016, Liaoning, China.
[3]Songshan Lake Materials Laboratory, Dongguan 523808, Guangdong, China.
[4]Institute of Physics, Chinese Academy of Sciences, Beijing 100190, China.
[#]Authors contributed equally.

Correspondence to: Prof. Yu-Jia Wang, Shenyang National Laboratory for Materials Science, Institute of Metal Research, 72 Wenhua Road, Shenyang 110016, Liaoning, China. E-mail: yjwang@imr.ac.cn

How to cite this article: Li HM, Zhang H, Wang YJ, Tang YL, Zhu YL, Ma XL. Misfit strain-misfit strain phase diagram of (110)-oriented ferroelectric $PbTiO_3$ films: a phase-field study. *Microstructures* 2024;4:2024004. https://dx.doi.org/10.20517/microstructures.2023.53

Received: 25 Sep 2023 **First Decision:** 3 Nov 2023 **Revised:** 3 Dec 2023 **Accepted:** 13 Dec 2023 **Published:** 9 Jan 2024

Academic Editor: Shujun Zhang **Copy Editor:** Fangling Lan **Production Editor:** Fangling Lan

Abstract

Ferroelectric thin films with high index orientations are found to possess unique structures and properties. In this work, we constructed the misfit strain-misfit strain phase diagram of (110)-oriented $PbTiO_3$ (PTO) thin films by phase-field simulations. The evolutions of ferroelectric phase structures, domain morphologies, volume fractions, and polarization components with the anisotropic strains were analyzed in detail. Large anisotropic strains exist between the orthorhombic scandate substrates and (110)-oriented PTO films, which makes it possible to engineer the structures and properties by anisotropic strain. These results deepen the understanding of ferroelectric domain structures of (110)-oriented PTO films under the anisotropic strain and provide theoretical support for the anisotropic strain engineering of high-index thin films experimentally.

Keywords: (110)-oriented $PbTiO_3$ film, phase-field simulation, anisotropic misfit strains, phase diagram, domain structures

INTRODUCTION

Ferroelectric materials have broad applications in the fields of sensors, actuators, and non-volatile memories[1-5] and have attracted abundant attention in recent years. How to regulate the excellent properties of ferroelectric materials is the focus of attention. In this process, researchers have tried many methods, such as strain[6-10], film thickness[11-13], electrical boundary condition[14,15], growth orientation[16-20], *etc*. Both experiments and theoretical simulations have proved that the ferroelectric thin films with high index orientations, such as (110)- and (111)-orientations, have unique structures and properties different from those with low index orientation, such as the (001)-orientation[21-26]. $PbTiO_3$ (PTO) is a prototypical ferroelectric material, which undergoes a cubic-to-tetragonal ferroelectric transition at about 765 K[27,28]. For (110)-oriented PTO films, the temperature-misfit strain phase diagrams[29] were constructed by the phenomenological theory, which indicates that various low-symmetry phases could emerge at different strain states. However, the phenomenological theory only considers single-domain states and prescribed multi-domain states. In contrast, the phase-field simulations could predict the optimal multi-domain structures under certain external conditions and their evolutions with the external field. In our previous work, the temperature-misfit strain phase diagram of the (110)-oriented PTO film was constructed by phase-field simulations, and the effects of epitaxial strain on the structures and properties were systematically investigated[30].

Due to the anisotropy of the crystal, the (110)-oriented ferroelectric films can exhibit unique properties. Experimentally, there are many orthogonal substrates that exert asymmetric in-plane strain. For example, the orthogonal $NdGaO_3$ substrate applies the asymmetric strain to the (110)-oriented $Ba_{1-x}Sr_xTiO_3$ film, resulting in strong in-plane dielectric anisotropy[17,31]. For ferroelectric PTO, the anisotropic misfit strain phase diagrams[32] were constructed by the phenomenological theory. However, there are no phase-field studies that could provide predictive anisotropic misfit strain multi-domain phase diagrams for experimentalists.

In this paper, the effect of asymmetric misfit strain on ferroelectric phase (domain) structures of (110)-orientated PTO films is constructed by analyzing the phase-field data via the stereographic projection (SP) method[30,33,34]. Then, the typical phase (domain) structures under asymmetric misfit strain states and their evolution with strain are analyzed in detail. Finally, it is pointed out that a series of orthogonal substrates can apply large asymmetric misfit strains to achieve the regulation of (110)-oriented PTO films. These results help to deepen the understanding of ferroelectric domain structures under high index asymmetric misfit strain and provide theoretical guidance for the design of ferroelectric devices based on asymmetric misfit strain regulation.

METHODS

Phase field model

The phase-field model suitable for the (110)-oriented ferroelectric films was constructed in our previous work[30]. Here, the main formulae were briefly outlined. A new coordinate system (x_1, x_2, x_3) with axes along the [100], [0$\bar{1}$1], and [011] directions is introduced along with the common one ($\tilde{x}_1$, $\tilde{x}_2$, $\tilde{x}_3$) with axes along the [100], [010], and [001] directions of a perovskite unit cell. The polarization components P_i in the coordinate system (x_1, x_2, x_3) are related to that in the coordinate system ($\tilde{x}_1$, $\tilde{x}_2$, $\tilde{x}_3$) via the transformation matrix T_{ij}:

$$P_i = T_{ij}\tilde{P}_j \tag{1}$$

where the transformation matrix T_{ij} can be written as follows:

$$T_{ij}=\begin{pmatrix}1 & 0 & 0\\ 0 & 1/\sqrt{2} & 1/\sqrt{2}\\ 0 & -1/\sqrt{2} & 1/\sqrt{2}\end{pmatrix} \tag{2}$$

The temporal evolution of P_i is modeled via numerically solving the time-dependent Ginzburg-Landau (TDGL) equation:

$$\frac{\partial P_i(x,t)}{\partial t}=-L\frac{\delta F}{\delta P_i(x,t)},(i=1,2,3), \tag{3}$$

where t is the time step, L is the kinetic coefficient related to the domain wall mobility, and the total free energy F consists of the following contributions:

$$F=\int_V[f_{bulk}(P_i)+f_{grad}(P_{i,j})+f_{elas}(P_i,\varepsilon_{ij})+f_{elec}(P_i,E_i)]dV \tag{4}$$

The first term is the bulk energy density,

$$\begin{aligned}f_{bulk}&=\alpha_1(P_1^2+P_2^2+P_3^2)+\alpha_{11}P_1^4+\alpha_{22}^*(P_2^4+P_3^4)+\alpha_{12}(P_1^2P_2^2+P_1^2P_3^2)\\&+\alpha_{23}^*P_2^2P_3^2+\alpha_{111}P_1^6+\alpha_{222}^*(P_2^6+P_3^6)+\alpha_{112}P_1^4(P_2^2+P_3^2)\\&+\alpha_{221}^*(P_2^4P_1^2+P_3^4P_1^2)+\alpha_{223}^*(P_2^4P_3^2+P_3^4P_2^2)+\alpha_{123}^*P_1^2P_2^2P_3^2\end{aligned} \tag{5}$$

where α_1 , α_{11} , α_{22}^* , α_{12} , α_{23}^* , α_{222}^* , α_{112} , α_{221}^* , α_{223}^* , and α_{123}^* are the Landau-Devonshire coefficients. The second term is gradient energy density,

$$\begin{aligned}f_{grad}&=\frac{1}{2}G_{11}P_{1,1}^2+\frac{1}{2}G_{22}^*(P_{2,2}^2+P_{3,3}^2)+G_{12}(P_{1,1}P_{2,2}+P_{1,1}P_{3,3})+G_{23}^*P_{2,2}P_{3,3}\\&+\frac{1}{2}G_{44}^*(P_{2,3}+P_{3,2})^2+\frac{1}{2}G_{55}^*[(P_{1,2}+P_{2,1})^2+(P_{1,3}+P_{3,1})^2]\end{aligned} \tag{6}$$

where G_{11} , G_{22}^*, G_{12} , G_{23}^*, G_{44}^*, and G_{55}^* are the gradient coefficients in Voigt's notation for the cubic system. The third term is elastic energy density,

$$\begin{aligned}f_{elas}&=\frac{1}{2}C_{11}e_{11}^2+\frac{1}{2}C_{22}^*(e_{22}^2+e_{33}^2)+C_{12}(e_{11}e_{22}+e_{11}e_{33})+C_{23}^*e_{22}e_{33}\\&+2C_{44}^*e_{23}^2+2C_{55}^*(e_{12}^2+e_{13}^2)\end{aligned} \tag{7}$$

where C_{ijkl} is the elastic stiffness tensor involving C_{11}, C_{22}^*, C_{12}, C_{23}^*, C_{44}^*, and C_{55}^* e_{ij} is elastic strain, the difference between the total strain ε_{ij} and the spontaneous strain ε_{ij}^0 The expression of spontaneous strain ε_{ij}^0 and the spontaneous polarization P_i can be written as follows.

$$\begin{aligned}\varepsilon_{11}^0 &= Q_{11}P_1^2 + Q_{12}(P_2^2 + P_3^2)\\ \varepsilon_{22}^0 &= Q_{12}P_1^2 + Q_{22}^*P_2^2 + Q_{23}^*P_3^2\\ \varepsilon_{33}^0 &= Q_{12}P_1^2 + Q_{23}^*P_2^2 + Q_{22}^*P_3^2\\ \varepsilon_{23}^0 &= Q_{44}^*P_2P_3\\ \varepsilon_{13}^0 &= Q_{55}^*P_1P_3\\ \varepsilon_{12}^0 &= Q_{55}^*P_1P_2\end{aligned} \tag{8}$$

where Q_{11}, Q_{12}, Q_{22}^*, Q_{23}^*, Q_{44}^*, and Q_{55}^* are the electrostrictive coefficients. The last term is electrostatic energy density,

$$f_{elec} = -\frac{1}{2}\varepsilon_0\varepsilon_b E_i^2 - E_i P_i \tag{9}$$

The thermodynamic parameters of PTO used in this paper refer to the previous literature[30] and are listed in Table 1. The conversion relationship between these coefficients and those under the (001) orientation is shown in Table 2. The coefficients with the superscript '*' denote those in the (110) orientation.

To construct the misfit strain-misfit strain phase diagram of (110)-oriented PTO films, we employed $128\Delta x \times 128\Delta y \times 60\Delta z$ discrete grid points with grid spacing $\Delta x = \Delta y = 1$ nm and $\Delta z = 0.4$ nm, which corresponds to $128 \times 128 \times 24$ nm^3 in the real space. The thickness of the PTO thin film and the deformable substrate are 20 and 4 nm, respectively. The in-plane misfit strains ε_{11} and ε_{22} range from -4% to 4%, and the temperature is chosen as the room temperature (25 °C). Periodic boundary conditions were applied along the in-plane directions. The mixed mechanical boundary condition was applied, ensuring that the top surface of the film is in a traction-free state, while the bottom of the simulation region in the substrate is fixed. The short-circuit electric boundary condition is considered where the electric potential at the top film surface and the film/substrate interface is fixed to zero. Random noise is used to simulate the annealing process as the initial setup. All related coefficients of PTO are adopted from the previous literature[7,35].

RESULTS AND DISCUSSION

Misfit strain-misfit strain phase diagram

A series of equilibrium structures under different misfit strains ε_{11} and ε_{22} are calculated by phase-field simulations. Firstly, the structures of (110)-oriented PTO films are analyzed via the SP method, and the type of phase at each position of misfit strain-misfit strain space is determined, as shown in Figure 1. There are several phases, including the tetragonal phase (T_a: $P_1 \neq 0$, $P_2 = P_3 = 0$, T_c: $P_2 = P_3 \neq 0$, $P_1 = 0$), the orthogonal phase (O_c: $P_3 \neq 0$, $P_1 = P_2 = 0$), the monoclinic phase (M_c: $P_2 \neq P_3 \neq 0$, $P_1 = 0$), and the rhombohedral phase (R: $P_1 \neq P_2 \neq 0$, $P_3 = 0$). The ranges of tetragonal-like, orthogonal, and rhombohedral-like phases are marked by green, red, and orange solid circles, respectively, with radii of 10°. The polarization vector of the monoclinic M_c phase rotates in the x_2-x_3 plane. When the angle between the polarization vector of the M_c phase and the original [001] axis is less than 10°, it is defined as the T_c phase. In fact, the T_c phase is a tetragonal-like monoclinic M_c phase. Comparing the SPs under each misfit strain with the ideal position schematic diagram of the (110)-oriented PTO ferroelectric phase shown in the center of Figure 1, the phase and polarization variants under different misfit strains can be determined accurately.

When the strain state of the PTO film is the symmetrical strain of $\varepsilon_{11} = \varepsilon_{22} = -4\%$, the peak of the projection point is located at the center of the SPs, as shown in Figure 1A, which indicates that the polarization vectors are parallel to the x_3 axis, that is, the O_c phase. Keeping ε_{11} at a compressive strain of -4% and changing ε_{22} toward the tensile strain gradually, the peak of the projection point splits into two parts along the x_2 axis, corresponding to the two polarized variants of the M_c phase, as shown in Figure 1B. When ε_{22} continues to

Table 1. Material parameters of $PbTiO_3$ used in the phase-field simulations

α_1	$3.8(T - 479) \times 10^5$	$C^{-2}\cdot m^2\cdot N$	Q_{11}	0.089	$C^{-2}\cdot m^4$
α_{11}	-7.3×10^7	$C^{-4}\cdot m^6\cdot N$	Q_{12}	-0.026	$C^{-2}\cdot m^4$
α_{12}	7.5×10^8	$C^{-4}\cdot m^6\cdot N$	Q_{44}	0.0675	$C^{-2}\cdot m^4$
α_{111}	2.6×10^8	$C^{-6}\cdot m^{10}\cdot N$	G_{11}	1.035×10^{-10}	$C^{-2}\cdot m^4\cdot N$
α_{112}	6.1×10^8	$C^{-6}\cdot m^{10}\cdot N$	G_{12}	0	$C^{-2}\cdot m^4\cdot N$
α_{123}	-3.7×10^9	$C^{-6}\cdot m^{10}\cdot N$	G_{44}	5.176×10^{-11}	$C^{-2}\cdot m^4\cdot N$
C_{11}	1.746×10^{11}	$N\cdot m^{-2}$	ε_b	40	
C_{12}	7.937×10^{10}	$N\cdot m^{-2}$			
C_{44}	1.111×10^{11}	$N\cdot m^{-2}$			

Table 2. The relations of the energy coefficients to transform from (001)-oriented coordinate systems to (110)-oriented coordinate systems

Landau-devonshire coefficients	$\alpha_{22}^* = (2\alpha_{11} + \alpha_{12})/4$, $\alpha_{23}^* = (6\alpha_{11} - \alpha_{12})/2$,
	$\alpha_{222}^* = (\alpha_{111} + \alpha_{112})/4$, $\alpha_{221}^* = (2\alpha_{112} + \alpha_{123})/4$,
	$\alpha_{223}^* = (15\alpha_{111} - \alpha_{112})/4$, $\alpha_{123}^* = (6\alpha_{112} - \alpha_{123})/2$
Gradient coefficients	$G_{22}^* = (G_{11} + G_{12} + 2G_{44})/2$,
	$G_{23}^* = (G_{11} + G_{12} - 2G_{44})/2$,
	$G_{44}^* = (G_{11} - G_{12})/2$, $G_{55}^* = G_{44}$
Elastic stiffness tensors	$C_{22}^* = (C_{11} + C_{12} + 2C_{44})/2$,
	$C_{23}^* = (C_{11} + C_{12} - 2C_{44})/2$,
	$C_{44}^* = (C_{11} - C_{12})/2$, $C_{55}^* = C_{44}$
Electrostrictive coefficients	$Q_{22}^* = (Q_{11} + Q_{12} + Q_{44}/2)/2$,
	$Q_{23}^* = (Q_{11} + Q_{12} - Q_{44}/2)/2$,
	$Q_{44}^* = 2(Q_{11} - Q_{12})$, $Q_{55}^* = Q_{44}$

increase to 4% of the tensile strain, the peaks of the M_c phase enter the range of the T_c phase, the green circles, as shown in Figure 1C. When ε_{22} is maintained at 4%, and ε_{11} is gradually changed toward the tensile strain, it is found that the peak of the M_c phase continues to deflect in the in-plane direction. When ε_{11} = 1%, the peaks of the T_a phase emerge at both ends of the x_1 axis, and the phase structure is T_a/M_c mixed phase, as shown in Figure 1D. Further increasing ε_{11}, the peaks of the R phase emerge. When the strain is $\varepsilon_{11} = \varepsilon_{22}$ = 4%, the peaks of the M_c phase disappear, resulting in the T_a/R phase, as shown in Figure 1E. Keeping ε_{11} at 4% and decreasing ε_{22}, it is found that the peak of the R phase gradually weakens, and the peak of the M_c phase begins to appear on the x_2 axis. When the strain state is ε_{11} = 4% and ε_{22} = 1%, the phase structure evolves into the T_a/M_c phase again, as shown in Figure 1F. With the decrease of ε_{22}, the peaks of the M_c phase gradually disappear, and the phase structure transforms into the pure T_a phase, as shown in Figure 1G. Finally, the compressive strain of ε_{22} is maintained at -4%, after which ε_{11} is gradually reduced. Under the asymmetric strain of ε_{11} = 0% and ε_{22} = -4%, the peak of the O_c phase appears in the central region of the SPs, forming the T_a/O_c phase, as shown in Figure 1H. As ε_{11} continues to change toward the compressive strain, the peaks of the T_a phase gradually weaken, and the phase structure transforms into a pure O_c phase, as shown in Figure 1A.

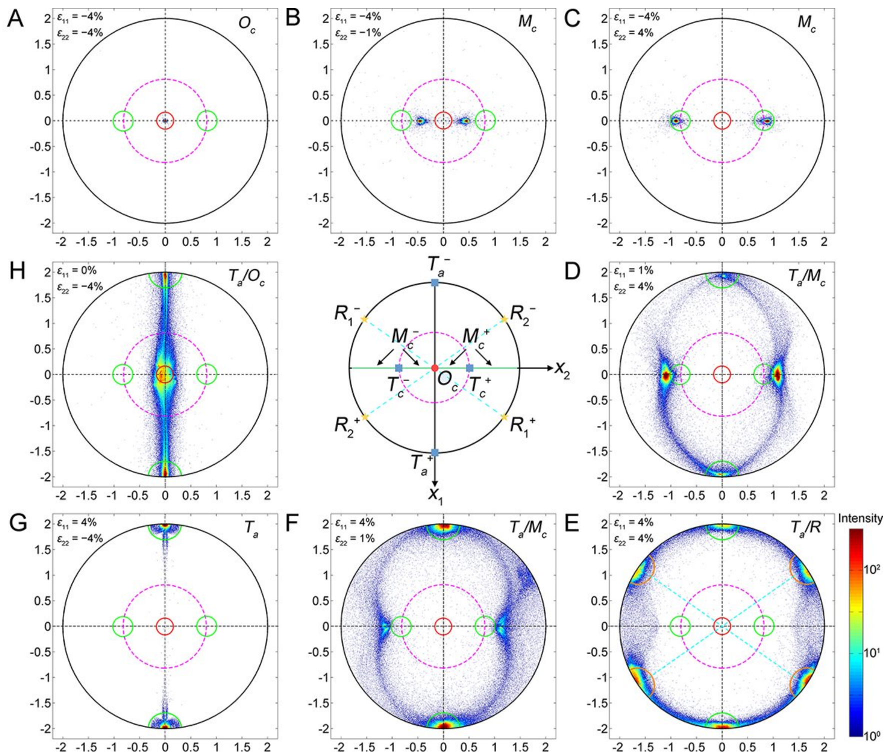

Figure 1. The stereographic projections of ferroelectric phases for (110)-oriented PTO thin films under anisotropic misfit strains at room temperature. (A-H) The stereographic projections of typical ferroelectric phases under different strain states. The schematic diagram in the center gives the ideal locations of different ferroelectric phases for (110)-oriented PTO films. The ranges of tetragonal-like, orthorhombic, and rhombohedral-like phases are marked by green, red, and orange solid circles. The magenta dashed circle indicates the position where the polarization vector deviates from the x_3 axis by 45°, and the cyan dashed lines mark the four in-plane <111> directions. The color reflects the intensity of the projection scatters.

Based on the above analysis, the misfit strain-misfit strain phase diagram of the (110)-oriented PTO film with a thickness of 20 nm at room temperature was constructed, as shown in Figure 2. It can be seen from the phase diagram that there are seven kinds of ferroelectric phases at room temperature. Under a large compressive strain (the left-bottom corner), an out-of-plane polarized O_c phase region appears. Under large asymmetric strains (the left-top and right-bottom corners), there are single-phase regions of the T_a phase and the M_c phase. In other regions, there are some mixed-phase regions, including the T_a/O_c, T_a/M_c, and $T_a/M_c/R$ phases. Compared with the misfit strain-misfit strain phase diagram of the (001)-oriented PTO film, the misfit strain-misfit strain phase diagram of the (110)-oriented PTO film is asymmetric[36], and the symmetries of the phases in the (110)-oriented PTO are also generally lower than those under the (001) orientation. Compared with the temperature-symmetric strain phase diagram of the (110)-oriented PTO film[30], it is found that the high-temperature T_a phase can be stabilized at room temperature under the asymmetric strain.

Typical domain structures under asymmetric strain

Figure 3 gives the typical domain structure in (110)-oriented PTO films under different strain states. Figure 3A shows the orthorhombic O_c phase under the large compressive strain in the x_1 and x_2 directions, which consists of two polar variants, $O_c^+(0, 0, +P_3)$ and $O_c^-(0, 0, -P_3)$, perpendicular to the interface of the film and the substrate. Figure 3B shows the monoclinic M_c phase under the compressive strain in the x_1 direction and the tensile strain in the x_2 direction, which consists of two polarized anti-parallel polarization variants, $M_{c2}^+(0, +P_2, -P_3)$ and $M_{c2}^-(0, -P_2, +P_3)$. Figure 3C is the tetragonal-like T_a phase under the tensile

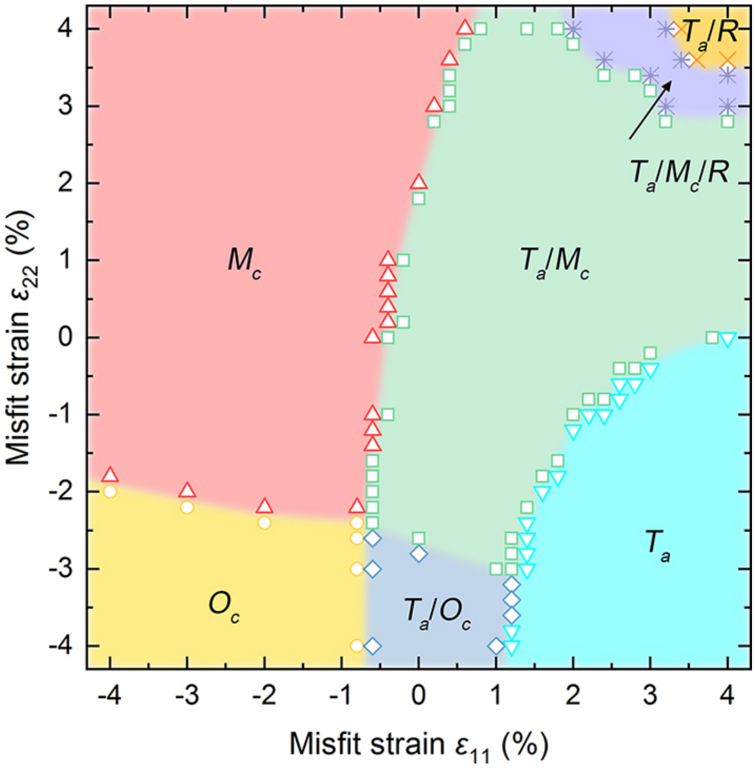

Figure 2. Misfit strain-misfit strain phase diagram of (110)-oriented PTO thin film at room temperature.

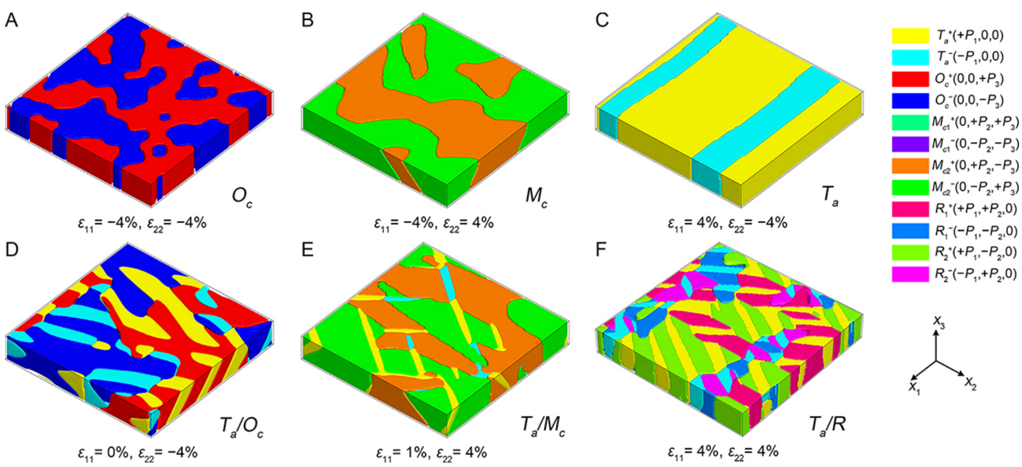

Figure 3. Typical domain structures of (110)-oriented PTO thin films under different misfit strains. (A) The O_c phase; (B) The M_c phase; (C) The T_a phase; (D) The T_a/O_c phase; (E) The T_a/M_c phase; (F) The T_a/R phase. The polarization variants are denoted by different colors, as labeled on the right.

strain in the x_1 direction and the compressive strain in the x_2 direction, which consists of two polarization variants, $T_a^+(+P_1, 0, 0)$ and $T_a^-(-P_1, 0, 0)$, with anti-parallel polarizations along the x_1 axis. These three single phases are all featured by 180° domain structures. The domain walls in the O_c phase are perpendicular to the interface, and the domain structures are maze-like. The domain wall in the M_c phase tilts to the interface, and the tilt angle changes with the asymmetric strain of the substrate. In contrast, the domain walls in the T_a phase are straight and perpendicular to the x_2 axis.

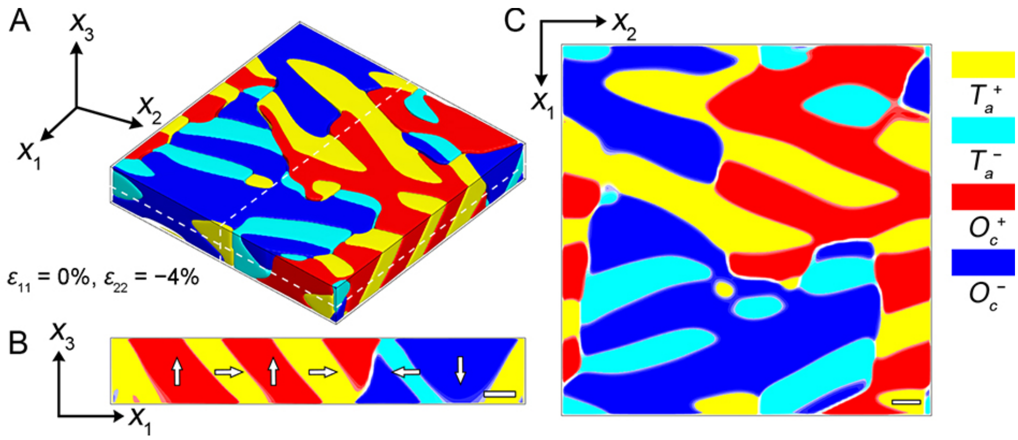

Figure 4. Domain structures of the T_a/O_c phase in (110)-oriented PTO thin films under the anisotropy strains of ε_{11} = 0% and ε_{22} = -4%. (A) The 3D domain structure; (B) The vertical cross-section; (C) The horizontal cross-section of the white dashed boxes in (A) The bars in (B and C) indicate 10 nm.

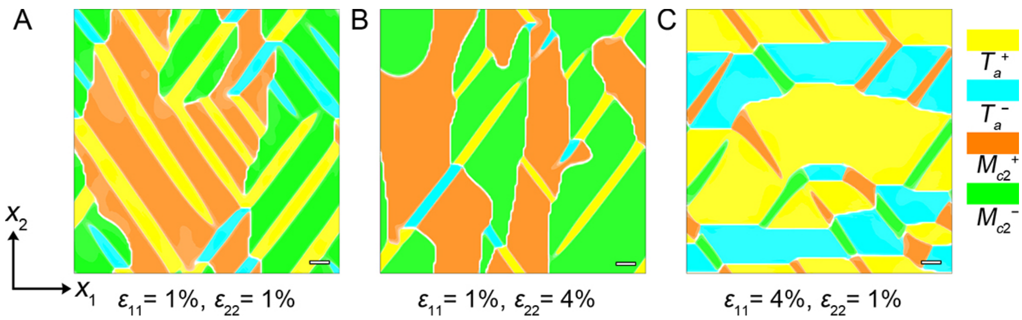

Figure 5. Domain morphologies of the T_a/M_c phase under different misfit strains. (A) ε_{11} = ε_{22} = 1.0%; (B) ε_{11} = 1.0%, ε_{22} = 4.0% and (C) ε_{11} = 4.0%, ε_{22} = 1.0%. The scale bars indicate 10 nm.

Figure 3D shows the T_a/O_c mixed phase under zero strain in the x_1 direction and large compressive strain in the x_2 direction. It contains two tetragonal variants, $T_a^+(+P_1, 0, 0)$, $T_a^-(-P_1, 0, 0)$, and two orthogonal variants, $O_c^+(0, 0, +P_3)$ and $O_c^-(0, 0, -P_3)$. The 90° ferroelastic domain wall is between the T_a phase and the O_c phase. The T_a/M_c mixed phase under a large tensile strain in the x_2 direction shown in Figure 3E contains two tetragonal variants, $T_a^+(+P_1, 0, 0)$ and $T_a^-(-P_1, 0, 0)$, and two monoclinic variants, $M_{c2}^+(0, +P_2, -P_3)$ and $M_{c2}^-(0, -P_2, +P_3)$. The T_a phase and the M_c phase are also separated by 90° ferroelastic phase boundaries. Under the asymmetric strain of ε_{11} = 1% and ε_{22} = 4%, fine stripes of the T_a phase are embedded in the M_c phase. Figure 3F is the T_a/R phase under a large symmetric tensile strain, which contains two kinds of tetragonal variants, $T_a^+(+P_1, 0, 0)$ and $T_a^-(-P_1, 0, 0)$, and four kinds of rhombohedral variants, $R_1^+(+P_1, +P_2, 0)$, $R_1^-(-P_1, -P_2, 0)$, $R_2^+(+P_1, -P_2, 0)$, and $R_2^-(-P_1, +P_2, 0)$. The detailed domain/phase structures and topological domains have been analyzed elaborately in the previous work[30].

Among the above-mentioned typical domain structures, the T_a/O_c phase is a newly emerged mixed phase under the asymmetric strain. Figure 4 shows the three-dimensional domain structure of the T_a/O_c phase and the cross-sectional view from different directions. From the vertical cross-section in Figure 4B, we can see the vertical and horizontal alternating domain structure and the inclined 90° domain wall, and the angle between the domain wall and the interface is about 50°. The reason that the angle deviates from 45° is that the polarization magnitudes of the T_a and O_c phases are not equal. The horizontal cross-section of Figure 4C reflects the irregular strip domain structure and 90° domain wall from another direction.

The effect of asymmetric strain on domain structures

In order to further reveal the effect of asymmetric strain on the domain structure of (110)-oriented PTO films, the domain structure and domain morphology of the T_a/M_c phase under different strains are analyzed in this section, as shown in Figure 5. Figure 5A shows the T_a/M_c phase structure under the symmetric strain of $\varepsilon_{11} = \varepsilon_{22} = 1\%$. The strip-like T_a phase and the M_c phase (the volume fraction is about 66.1%) coexist, and the domain wall density is high. When increasing the strain in the x_2 direction to $\varepsilon_{22} = 4\%$, as shown in Figure 5B, the volume fraction of the M_c phase increases (about 88.3%) at the expanse of the strip T_a phase. When increasing the strain in the x_1 direction to $\varepsilon_{11} = 4\%$, however, the volume fraction of the T_a phase increases while that of the M_c phase decreases (about 9.3%), as shown in Figure 5C.

Figure 6 is the evolution of the phase structure with the strain ε_{11} under fixed ε_{22}. When $\varepsilon_{22} = -2\%$, it can be seen from Figure 6A that with the increase of ε_{11}, the phase structure undergoes the evolution path of $O_c \rightarrow M_c \rightarrow T_a/M_c \rightarrow T_a$. In the T_a/M_c phase region, with the increase of ε_{11}, the volume fraction of the T_a phase increases, and the volume fraction of the M_c phase decreases. Figure 6B is the corresponding polarization component evolution diagram. With the increase of ε_{11}, the out-of-plane P_z component gradually decreases, and the in-plane P_y component gradually increases. At $\varepsilon_{11} = 2\%$, due to the disappearance of the M_c phase, the P_y and P_z components decrease to zero. The in-plane P_x component appears at $\varepsilon_{11} = -1\%$ and gradually increases with the increase of misfit strain ε_{11}. Corresponding to the volume fraction diagram, in the strain range of $\varepsilon_{11} = -1\%$-2%, it is a T_a/M_c mixed phase with three polarization components. Figure 6C is the angle evolution diagram between the polarization of the $M_c(O_c)$ phase and the x_3 axis. The polarization angle increases from 4 to 25°, indicating that the polarization vector gradually rotates to the in-plane direction with the increase of ε_{11}. In addition, we also analyzed the evolution of phase volume fractions, polarization components, and polarization angles with the misfit strain ε_{11} when $\varepsilon_{22} = 0\%$ and $\varepsilon_{22} = 2\%$, as shown in Figure 6D-F and G-I, respectively. At $\varepsilon_{22} = 0\%$, with the increase of ε_{11}, the evolution path of the phase is $M_c \rightarrow T_a/M_c \rightarrow T_a$, as shown in Figure 6D. At $\varepsilon_{22} = 2\%$, with the increase of ε_{11}, the evolution path is $M_c \rightarrow T_a/M_c$, as shown in Figure 6G. The corresponding polarization component diagrams [Figure 6E and H] and polarization angle diagrams [Figure 6F and I] have similar evolution trends as those of $\varepsilon_{22} = -2\%$. With the increase of ε_{11}, the out-of-plane P_z component corresponding to M_c gradually decreases, and the in-plane P_y component gradually increases. The P_x component corresponding to T_a increases gradually. Similarly, the angle between the M_c phase and the x_3 axis is also increasing, indicating that the polarization of the M_c phase rotates to the in-plane direction.

Figure 7 is the evolution of the phase structure with the misfit strain ε_{22} when the misfit strain ε_{11} is fixed. At $\varepsilon_{11} = -2\%$, with the increase of ε_{22}, the phase structure evolves from the O_c phase to the M_c phase, as shown in Figure 7A. Figure 7B reflects the evolution of the polarization component. When $\varepsilon_{22} = -3\%$, the in-plane P_y component emerges and gradually increases with ε_{22}, while the out-of-plane P_z component increases first and then decreases. Figure 7C shows the change of the angle between the polarization of the $M_c(O_c)$ phase and the x_3 axis. In the M_c phase region, the angle increases from 0 to 51.5°, indicating that the polarization of the M_c phase gradually rotates to the in-plane direction with the increase of ε_{22}. At $\varepsilon_{11} = 0\%$, it can be seen from the phase volume fraction in Figure 7D that with the increase of ε_{22}, the evolution path is $T_a/O_c \rightarrow T_a/M_c \rightarrow M_c$. In the T_a/M_c phase region, with the increase of ε_{22}, the volume fraction of the T_a phase decreases, and that of the M_c phase increases. As shown in Figure 7E, the variation trends of P_y and P_z components are the same as that in the case of $\varepsilon_{11} = -2\%$ [Figure 7B]. In addition, the P_x component corresponding to T_a gradually increases with strains and disappears at $\varepsilon_{22} = 2\%$. At $\varepsilon_{11} = 2\%$, with the increase of ε_{22}, the evolution path of the phase is $T_a \rightarrow T_a/M_c \rightarrow T_a/M_c/R$, as shown in Figure 7G. Figure 7H shows that in the range of $\varepsilon_{22} < -2\%$, there is only the P_x component corresponding to T_a, and its polarization magnitude does not change significantly with the increase of strain. When $\varepsilon_{22} = -2\%$, the M_c phase appears, and its corresponding P_y and P_z components also increase suddenly. With the increase of ε_{22}, the in-plane P_x and P_y

Table 3. The lattice constants of commonly used orthorhombic scandate and gallate substrates and the misfit strains between these substrates and (110)-oriented PTO films

Substrate	*a*/Å	*b*/Å	*c*/Å	$(100)_O$ substrate		$(010)_O$ substrate	
				$[100]//[001]_O$	$[011]//[010]_O$	$[100]//[001]_O$	$[011]//[100]_O$
$DyScO_3$	5.440	5.717	7.903	-0.14%	2.16%	-0.14%	-2.79%
$TbScO_3$	5.466	5.731	7.917	0.04%	2.41%	0.04%	-2.32%
$GdScO_3$	5.480	5.746	7.932	0.23%	2.68%	0.23%	-2.07%
$SmScO_3$	5.527	5.758	7.965	0.64%	2.89%	0.64%	-1.23%
$NdScO_3$	5.575	5.776	8.003	1.12%	3.22%	1.12%	-0.38%
$PrScO_3$	5.608	5.780	8.025	1.40%	3.29%	1.40%	0.21%
$NdGaO_3$	5.433	5.504	7.716	-2.50%	-1.64%	-2.50%	-2.91%
$PrGaO_3$	5.459	5.493	7.732	-2.30%	-1.84%	-2.30%	-2.45%
$LaGaO_3$	5.494	5.527	7.778	-1.72%	-1.23%	-1.72%	-1.82%

In this work, two orthorhombic orientations $(100)_O$ and $(010)_O$ of these substrates are considered, where the subscript O denotes orthorhombic indices. The in-plane lattice constants in the [100] and [011] directions of the (110)-oriented PTO film are 3.957 and 5.596 Å, respectively.

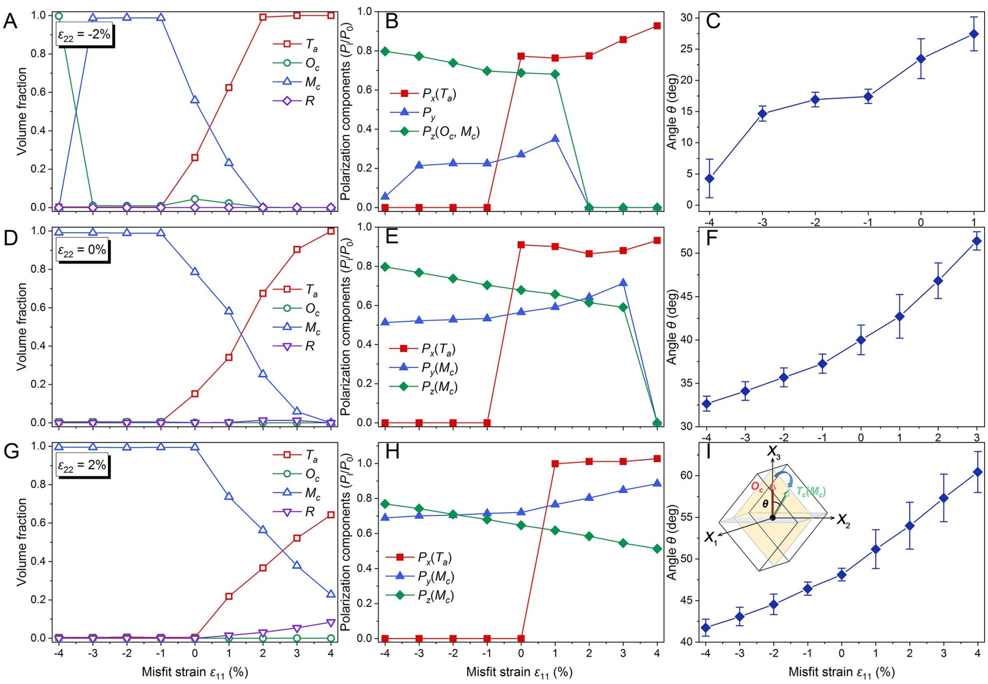

Figure 6. Phase structure evolutions of (110)-oriented PTO films with respective to misfit strain ε_{11} at various constant strain ε_{22}. (A-C) ε_{22} = -2%; (D-F) ε_{22} = 0%; (G-I) ε_{22} = 2%. (A, D, G) are the volume fractions. (B, E, H) are the polarization components of various phases. (C, F, I) are the angle θ between the polarizations of the $M_c(O_c)$ phase and the x_3 axis, in which the bars represent the standard deviations of the angle. The schematic of the angle θ is shown as an insert in (I).

components gradually increase, and the out-of-plane P_z component gradually decreases. When ε_{22} = 4%, the $P_x(R)$ and $P_y(R)$ components corresponding to the R phase appear. Similarly, the polarization angle diagram of the M_c phase [Figure 7F and I] also reflects the evolution of the M_c phase with the increase of strain ε_{22}.

Asymmetric strain between the orthogonal substrates and the film

In recent years, with the development of a series of commercial orthogonal substrates, it is possible to control the domain structure in (110)-oriented PTO films by the asymmetric strain. The lattice constants of the commonly used orthorhombic scandate and gallate substrates and the mismatch strain between them

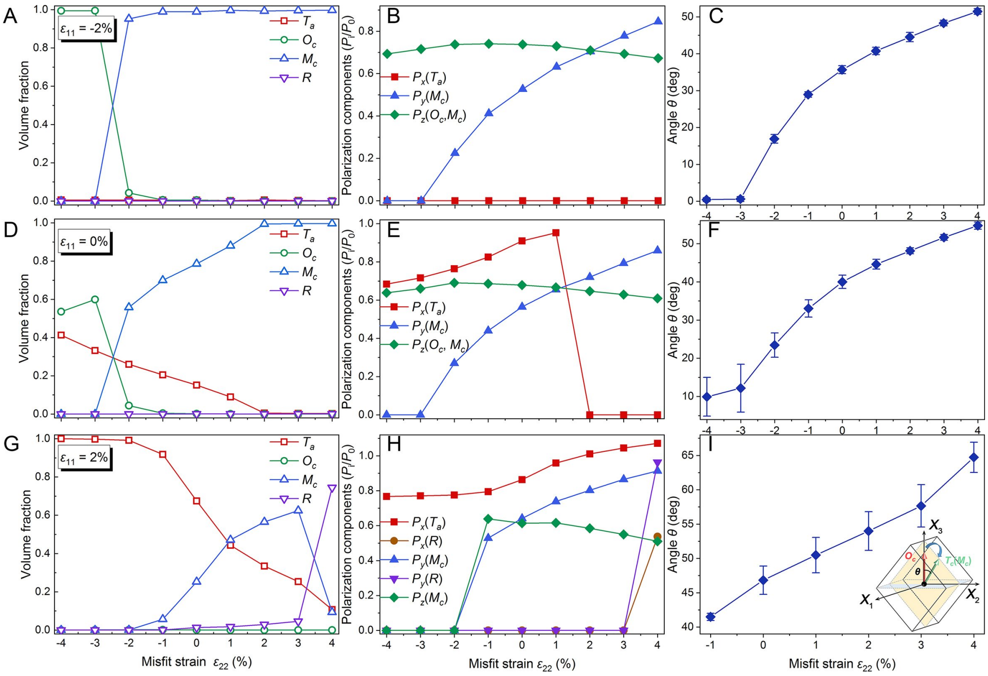

Figure 7. Phase structure evolutions of (110)-oriented PTO films with respective to misfit strain ε_{22} at various constant strains ε_{11}. (A-C) ε_{11} = -2%; (D-F) ε_{11} = 0%; (G-I) ε_{11} = 2%. (A, D, G) are the volume fractions. (B, E, H) are the polarization components of various phases. (C, F, I) are the angle θ between the polarizations of the $M_c(O_c)$ phase and the x_3 axis, in which the bars represent the standard deviations of the angle.

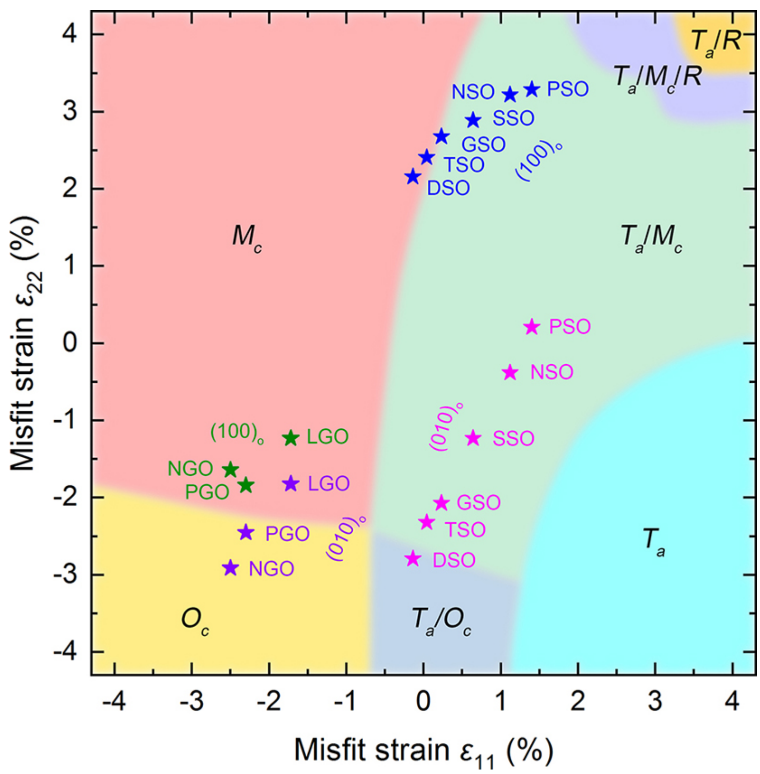

Figure 8. The strain positions of orthorhombic scandate and gallate substrates in the phase diagram.

and the (110)-oriented PTO film are listed in Table 3. In the phase-field simulation, the lattice constants of the (110)-oriented PTO film in the in-plane $x_1[100]$ and $x_2[011]$ directions are a_c = 3.957 Å and $\sqrt{2}a_c$ = 5.596 Å, respectively. In order to make the (110)-oriented film and the orthogonal substrate match the lattice in two directions in the interface, there are two growth orientations. One is grown on the $(100)_O$ plane, which satisfies $[100]_{PC}//[001]_O$, $[011]_{PC}//[010]_O$. The other one is grown on the $(010)_O$ plane, which satisfies $[100]_{PC}//[001]_O$, $[011]_{PC}//[100]_O$, where the subscripts PC and O represent the pseudo-cubic index of the film and the orthogonal index of the substrate, respectively. The misfit strains corresponding to the orthogonal $(100)_O$ and $(010)_O$ scandate and gallate substrates are plotted in the phase diagram, as shown in Figure 8. It can be seen that the strains corresponding to the $(100)_O$- and $(010)_O$-oriented scandate substrates are located in the T_a/M_c, T_a/O_c, and M_c phase regions. The strains corresponding to the $(100)_O$- and $(010)_O$-oriented gallate substrates are located near the phase boundary between the O_c phase and the M_c phase.

CONCLUSIONS

In this work, the misfit strain-misfit strain multi-domain phase diagram of (110)-oriented PTO thin films at room temperature was constructed by phase-field simulations. Three single phases and four mixed phases were predicted to exist due to the anisotropic strain. The single phases (O_c and M_c) mainly exist within the phase region characterized by compressive ε_{11}, and the phase T_a, which is typically observed only at high temperatures under the isotropic strain conditions, emerges within the phase region marked by the tensile ε_{11} and the compressive ε_{22} at room temperature. The locations of various orthorhombic substrates marked in the phase diagram and the analysis of the polarization rotation should provide scientific guidance for the future development of piezoelectric devices.

DECLARATIONS

Authors' contributions

Data analysis, interpretation, initial draft writing, and manuscript revision: Li HM
Data acquisition: Zhang H
Manuscript revision; funding acquisition: Wang YJ
Funding acquisition: Tang YL, Zhu YL, Ma XL

Availability of data and materials

The data that support the findings of this study are available from the corresponding author upon reasonable request.

Financial support and sponsorship

This work is supported by the National Natural Science Foundation of China (52122101 and 51971223) and Shenyang National Laboratory for Materials Science (L2019R06, L2019R08, L2019F01, L2019F13). Wang YJ and Tang YL acknowledge the Youth Innovation Promotion Association CAS (2021187 and Y202048). Tang YL acknowledges the Scientific Instrument Developing Project of CAS (YJKYYQ20200066). We are grateful to Prof. Li J. Y. at Southern University of Science and Technology and Dr. Lei C. H. at Saint Louis University for the development of the phase-field code.

Conflicts of interest

All authors declared that there are no conflicts of interest.

Ethical approval and consent to participate

Not applicable.

Consent of publication

Not applicable.

REFERENCES

1. Muralt P. Ferroelectric thin films for micro-sensors and actuators: a review. *J Micromech Microeng* 2000;10:136. DOI
2. Setter N, Damjanovic D, Eng L, et al. Ferroelectric thin films: review of materials, properties, and applications. *J Appl Phys* 2006;100:051606. DOI
3. Scott JF. Applications of modern ferroelectrics. *Science* 2007;315:954-9. DOI PubMed
4. Hoffman J, Pan X, Reiner JW, et al. Ferroelectric field effect transistors for memory applications. *Adv Mater* 2010;22:2957-61. DOI
5. Martin LW, Rappe AM. Thin-film ferroelectric materials and their applications. *Nat Rev Mater* 2016;2:16087. DOI
6. Pertsev NA, Zembilgotov AG, Tagantsev AK. Effect of mechanical boundary conditions on phase diagrams of epitaxial ferroelectric thin films. *Phys Rev Lett* 1998;80:1988. DOI
7. Li YL, Hu SY, Liu ZK, Chen LQ. Effect of substrate constraint on the stability and evolution of ferroelectric domain structures in thin films. *Acta Mater* 2002;50:395-411. DOI
8. Schlom DG, Chen LQ, Eom CB, Rabe KM, Streiffer SK, Triscone JM. Strain tuning of ferroelectric thin films. *Annu Rev Mater Res* 2007;37:589-626. DOI
9. Damodaran AR, Agar JC, Pandya S, et al. New modalities of strain-control of ferroelectric thin films. *J Phys Condens Matter* 2016;28:263001. DOI
10. Damodaran AR, Pandya S, Agar JC, et al. Three-state ferroelastic switching and large electromechanical responses in $PbTiO_3$ thin films. *Adv Mater* 2017;29:1702069. DOI
11. Sheng G, Hu JM, Zhang JX, Li YL, Liu ZK, Chen LQ. Phase-field simulations of thickness-dependent domain stability in $PbTiO_3$ thin films. *Acta Mater* 2012;60:3296-301. DOI
12. Nesterov O, Matzen S, Magen C, Vlooswijk AHG, Catalan G, Noheda B. Thickness scaling of ferroelastic domains in $PbTiO_3$ films on $DyScO_3$. *Appl Phys Lett* 2013;103:142901. DOI
13. Li S, Zhu YL, Tang YL, et al. Thickness-dependent a_1/a_2 domain evolution in ferroelectric $PbTiO_3$ films. *Acta Mater* 2017;131:123-30. DOI
14. Nelson CT, Winchester B, Zhang Y, et al. Spontaneous vortex nanodomain arrays at ferroelectric heterointerfaces. *Nano Lett* 2011;11:828-34. DOI
15. Wang YJ, Feng YP, Zhu YL, et al. Polar meron lattice in strained oxide ferroelectrics. *Nat Mater* 2020;19:881-6. DOI
16. Tagantsev AK, Pertsev NA, Muralt P, Setter N. Strain-induced diffuse dielectric anomaly and critical point in perovskite ferroelectric thin films. *Phys Rev B* 2001;65:012104. DOI
17. Simon WK, Akdogan EK, Safari A, Bellotti JA. In-plane microwave dielectric properties of paraelectric barium strontium titanate thin films with anisotropic epitaxy. *Appl Phys Lett* 2005;87:082906. DOI
18. Ouyang J, Slusker J, Levin I, et al. Engineering of self-assembled domain architectures with ultra-high piezoelectric response in epitaxial ferroelectric films. *Adv Funct Mater* 2007;17:2094-100. DOI
19. Cao Y, Sheng G, Zhang JX, et al. Piezoelectric response of single-crystal $PbZr_{1-x}Ti_xO_3$ near morphotropic phase boundary predicted by phase-field simulation. *Appl Phys Lett* 2010;97:252904. DOI
20. Xu R, Karthik J, Damodaran AR, Martin LW. Stationary domain wall contribution to enhanced ferroelectric susceptibility. *Nat Commun* 2014;5:3120. DOI PubMed
21. Gui Z, Prosandeev S, Bellaiche L. Properties of epitaxial (110) $BaTiO_3$ films from first principles. *Phys Rev B* 2011;84:214112. DOI
22. Xu R, Zhang J, Chen Z, Martin LW. Orientation-dependent structural phase diagrams and dielectric properties of $PbZr_{1-x}TixO_3$ polydomain thin films. *Phys Rev B* 2015;91:144106. DOI
23. Lee JH, Chu K, Kim KE, Seidel J, Yang CH. Out-of-plane three-stable-state ferroelectric switching: finding the missing middle states. *Phys Rev B* 2016;93:115142. DOI
24. Feng YP, Jiang RJ, Zhu YL, et al. Strain coupling of ferroelastic domains and misfit dislocations in [101]-oriented ferroelectric $PbTiO_3$ films. *RSC Adv* 2018;12:20423-31. DOI
25. Xu R, Gao R, Reyes-Lillo SE, et al. Reducing coercive-field scaling in ferroelectric thin films *via* orientation control. *ACS Nano* 2018;12:4736-43. DOI
26. Feng YP, Tang YL, Zhu YL, Zou MJ, Wang YJ, Ma XL. Thickness-dependent evolution of piezoresponses and *a/c* domains in -oriented $PbTiO_3$ ferroelectric films. *J Appl Phys* 2020;128:224102. DOI
27. Cohen RE. Origin of ferroelectricity in perovskite oxides. *Nature* 1992;358:136-8. DOI
28. Jung WW, Lee HC, Ahn WS, Ahn SH, Choi SK. Switchable single c-domain formation in a heteroepitaxial $PbTiO_3$ thin film on a (001) Nb-$SrTiO_3$ substrate fabricated by means of hydrothermal epitaxy. *Appl Phys Lett* 2005;86:252901. DOI
29. Mtebwa M, Tagantsev AK, Yamada T, Gemeiner P, Dkhil B, Setter N. Single-domain (110) $PbTiO_3$ thin films: thermodynamic theory

and experiments. *Phys Rev B* 2016;93:144113. DOI

30. Zhang H, Feng YP, Wang YJ, Tang Y, Zhu Y, Ma X. Strain phase diagram and physical properties of (110)-oriented $PbTiO_3$ thin films by phase-field simulations. *Acta Mater* 2022;228:117761. DOI
31. Akcay G, Misirlioglu IB, Alpay SP. Dielectric tunability of (110) oriented barium strontium titanate epitaxial films on (100) orthorhombic substrates. *Appl Phys Lett* 2006;89:042903. DOI
32. Ma W, Wang F. Effect of in-plane strain anisotropy on (011) epitaxial $BaTiO_3$ and $PbTiO_3$ thin films. *AIP Adv* 2017;7:105120. DOI
33. Guo XW, Wang YJ, Zhang H, Tang YL, Zhu YL, Ma XL. Misfit strain-temperature phase diagram of multi-domain structures in (111)-oriented ferroelectric $PbTiO_3$ films. *Acta Mater* 2020;196:539-48. DOI
34. Guo XW, Zou MJ, Wang YJ, Tang Y, Zhu YL, Ma X. Effects of anisotropic misfit strains on equilibrium phases and domain structures in (111)-oriented ferroelectric $PbTiO_3$ films. *Acta Mater* 2021;206:116639. DOI
35. Chen LQ. Phase-field method of phase transitions/domain structures in ferroelectric thin films: a review. *J Am Ceram Soc* 2008;91:1835-44. DOI
36. Sheng G, Zhang JX, Li YL, et al. Domain stability of $PbTiO_3$ thin films under anisotropic misfit strains: Phase-field simulations. *J Appl Phys* 2008;104:054105. DOI